Journal of Colloid and Interface Science 594 (2021) 669–680

Contents lists available at ScienceDirect

Journal of Colloid and Interface Science

journal homepage: www.elsevier.com/locate/jcis

Regular Article

# Design and synthesis of an azobenzene–betaine surfactant for photo-rheological fluids

Calum S.G. Butler [a], Joshua P. King [a], Luke W. Giles [a], Joshua B. Marlow [a], Mark Louis P. Vidallon [a], Anna Sokolova [b], Liliana de Campo [b], Kellie L. Tuck [a,*], Rico F. Tabor [a,*]

[a] School of Chemistry, Monash University, Clayton, VIC 3800, Australia
[b] Australian Centre for Neutron Scattering, ANSTO, Lucas Heights, New South Wales 2234, Australia

## GRAPHICAL ABSTRACT

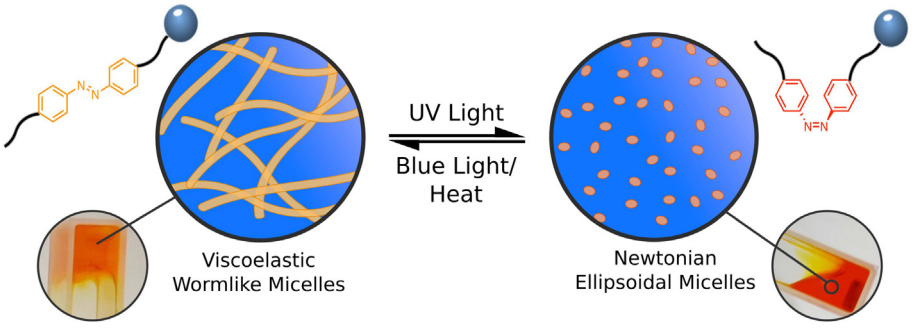


## ARTICLE INFO

*Article history:*
Received 26 November 2020
Revised 22 January 2021
Accepted 13 February 2021
Available online 24 February 2021

*Keywords:*
Wormlike micelles
Neutron scattering
Light responsive
Self-assembly
pi-pi interaction
Azobenzene
Rheology
Surfactant
Betaine

## ABSTRACT

*Hypothesis:* Morphology of surfactant self-assemblies are governed by the intermolecular interactions and packing constraints of the constituent molecules. Therefore, rational design of surfactant structure should allow targeting of the specific self-assembly modes, such as wormlike micelles (WLMs). By inclusion of an appropriate photo-responsive functionality to a surfactant molecule, light-based control of formulation properties without the need for additives can be achieved.

*Experiments:* A novel azobenzene-containing surfactant was synthesised with the intention of producing photo-responsive wormlike micelles. Aggregation of the molecule in its *cis* and *trans* isomers, and its concomitant flow properties, were characterised using UV–vis spectroscopy, small-angle neutron scattering, and rheological measurements. Finally, the fluids capacity for mediating particle diffusion was assessed using dynamic light scattering.

*Findings:* The *trans* isomer of the novel azo-surfactant was found to form a viscoelastic WLM network, which transitioned to inviscid ellipsoidal aggregates upon photo-switching to the *cis* isomer. This was accompanied by changes in zero-shear viscosity up to 16,000×. UV–vis spectroscopic and rheo-SANS analysis revealed $\pi - \pi$ interactions of the *trans* azobenzene chromophore within the micelles, influencing aggregate structure and contributing to micellar rigidity. Particles dispersed in a 1 wt% surfactant solution showed a fivefold increase in apparent diffusion coefficient after UV-irradiation of the mixture.



* Corresponding authors.
*E-mail addresses:* kellie.tuck@monash.edu (K.L. Tuck), rico.tabor@monash.edu (R.F. Tabor).

https://doi.org/10.1016/j.jcis.2021.02.061
0021-9797/

## 1. Introduction

Stimuli-responsive materials provide unparalleled versatility by allowing fine control and modulation of system functionality, and, as such, have found application in a variety of established and emerging fields [1–5]. Though the applications of many such systems manifest on a macroscopic scale, their unique properties are driven by interactions and rearrangements on a molecular level. In order to develop responsive materials effectively, a clear understanding of how changes in molecular architecture will modulate self-assembly, and thereby influence the nano-, micro- and macro-scale properties of these materials, is required.

Photo-rheological fluids (PRFs) are materials capable of changing their flow behaviour (rheological properties) upon irradiation with light of a specific wavelength [6]. Light is a particularly attractive stimulus as it is cheap, non-destructive, environmentally friendly and can be easily applied with fine spatiotemporal control [7–10]. PRFs promise a diverse array of applications in areas such as oil drilling [11], drag reduction [12], bio-separations [13] and templated synthesis [14]. Most PRFs are surfactant formulations that modulate their rheology and viscoelasticity by formation or disruption of an entangled wormlike micelle (WLM) network, and comprise a complex mixtures of surfactants, salts and photo-responsive additives [15–17]. While effective, the specificity and complexity of these formulations makes them sensitive to small changes in conditions or composition, resulting in tight windows of useful behaviour and limiting their application beyond proof-of-concept studies. To address this, it has remained an active goal to develop more simple and robust PRF formulations, ideally comprising only a single component in water [18].

The aggregation properties of surfactants are broadly governed by their steric packing parameter (*P*, Fig. 1a), as first proposed by Israelachvili et al. [19]. As such, development of a single-component PRF requires precise tuning of surfactant architecture to induce formation of WLMs, and inclusion of a functionality that allows light-induced control of said WLM formation, or entanglement. Control of aggregate behaviour is elicited by modulation of the surfactants packing parameter through the switching of the incorporated light responsive functionality. The technical challenges posed by these requirements mean that reports of single-component photo-rheological fluids that function at low concentrations are rare [20,21], and such systems tend to be discovered serendipitously rather than by molecular design. The design criteria required to induced the desired modes of self-assembly and allow effective photo-control of the aggregates remain outstanding research questions.

Azobenzenes are a class of photo-responsive chromophore that can undergo a reversible, light induced *trans* to *cis* isomerisation (Fig. 1b). The *trans* to *cis* isomerisation can be accessed by excitation of the $\pi \rightarrow \pi^*$ electronic transition (≈350 nm) and the reverse isomerisation either by excitation of the $n \rightarrow \pi^*$ transition of the *cis* isomer (≈450 nm) or heating of the molecule [22]. These easily accessible and well resolved transitions, alongside their ease of synthesis, relative stability and potential for enzymatic cleavage [23,24], have resulted in azobenzene being used to introduce photo-responsive properties to a variety of colloidal systems [25,26,18,27]. Inclusion of an azobenzene within an appropriate amphiphilic structure enables amplification their photo-induced change in molecular geometry, giving control of the surfactants packing parameter and therefore its aggregation properties [28]. Applied correctly, the azobenzene chromophore provides an ideal functionality for the generation of PRFs and photo-responsive colloids more generally. Despite their widespread use in a variety of well characterised micellar systems, the mechanistic influence of the azobenzene and its photo-switching on WLM aggregation remains largely unexplored.

The present work builds upon recent research in azo-surfactant design and analysis [29–31] and details the rational design, synthesis, self-assembly and rheological properties of a novel betaine-based azo-surfactant, capable of forming a highly functional photo-rheological fluid as a single-component in water. This molecule provides an excellent example of the efficacy of rational surfactant design when seeking to develop novel functional formulations. Furthermore, study of the self-assembly properties of this molecule has provided unprecedented insight into the self-assembly properties of azobenzene containing surfactants, their mode of action in formulation, and azobenzene's influence on both micro- and macroscopic properties of formulations. These discoveries highlight previously unexplored aspects of surfactant design and lay the groundwork for further novel formulation development.

## 2. Materials and methods

### 2.1. Materials

All synthetic materials were purchased at ⩾95% purity from Sigma–Aldrich or Merck and were used without further purification. Deuterated solvents for NMR were purchased from Cambridge Isotope Laboratories Inc. Normal phase flash chromatography was performed using Merck silica gel 60, 40–63 μm (mesh). Reverse phase flash chromatography was performed using reversed-phase silica (C18 bonded, 10 micron 60) purchased from Grace Davison. Thin-layer chromatography (TLC) was performed using TLC Silica Gel 60 F254 and visualised under UV light (254 nm).

### 2.2. General methods

#### 2.2.1. Neutron scattering

Static small-angle neutron scattering (SANS) measurements were obtained on the Bilby beam-line [32,33] in time-of-flight mode with an asymmetric detector array at the Australian Centre for Neutron Scattering (ACNS), ANSTO, Lucas Heights, NSW. A neutron wavelength of 6 Å was used in these measurements, obtaining a *q*-range of 0.003280.47555 Å. Samples were prepared in 1 mm path-length demountable quartz cells. Contrast was introduced by using deuterated $D_2O$ as the solvent. Raw scattering counts were normalised against a blocked beam and a transmission measurement, then were reduced to average absolute intensity profiles as a function of the momentum transfer or scattering vector, *q*, defined as:

$$q = \frac{4\pi}{\lambda} \sin\left(\frac{\theta}{2}\right) \quad (1)$$

where $\lambda$ is the de Broglie wavelength of the neutron and $\theta$ is the scattering angle. Rheology coupled to small-angle neutron scattering (rheo-SANS) measurements were performed on the Bilby beamline in a monochromatic mode using an Anton-Paar MCR 500 rheometer mounted in the path of the beam. A neutron wavelength of 6 Å was used in these measurements, obtaining a *q*-range of 0.007480.13850 Å. A specially made quartz Searle cell was used with an internal gap of 0.5 mm (total sample path length 1 mm) and a total sample volume of 6 mL. Reduced rheo-SANS data were analysed using a specially written MATLAB script to extract annular and sector information to detect anisotropy.

Ultra-small-angle neutron scattering (USANS) measurements were made using the Kookaburra beamline at the Australian Centre for Neutron Scattering, ANSTO [34,35]. The instrument features a Bonse-Hart setup in which two parallel arrays (one rotational) of quintuple-reflection channel-cut silicon crystals monochromate

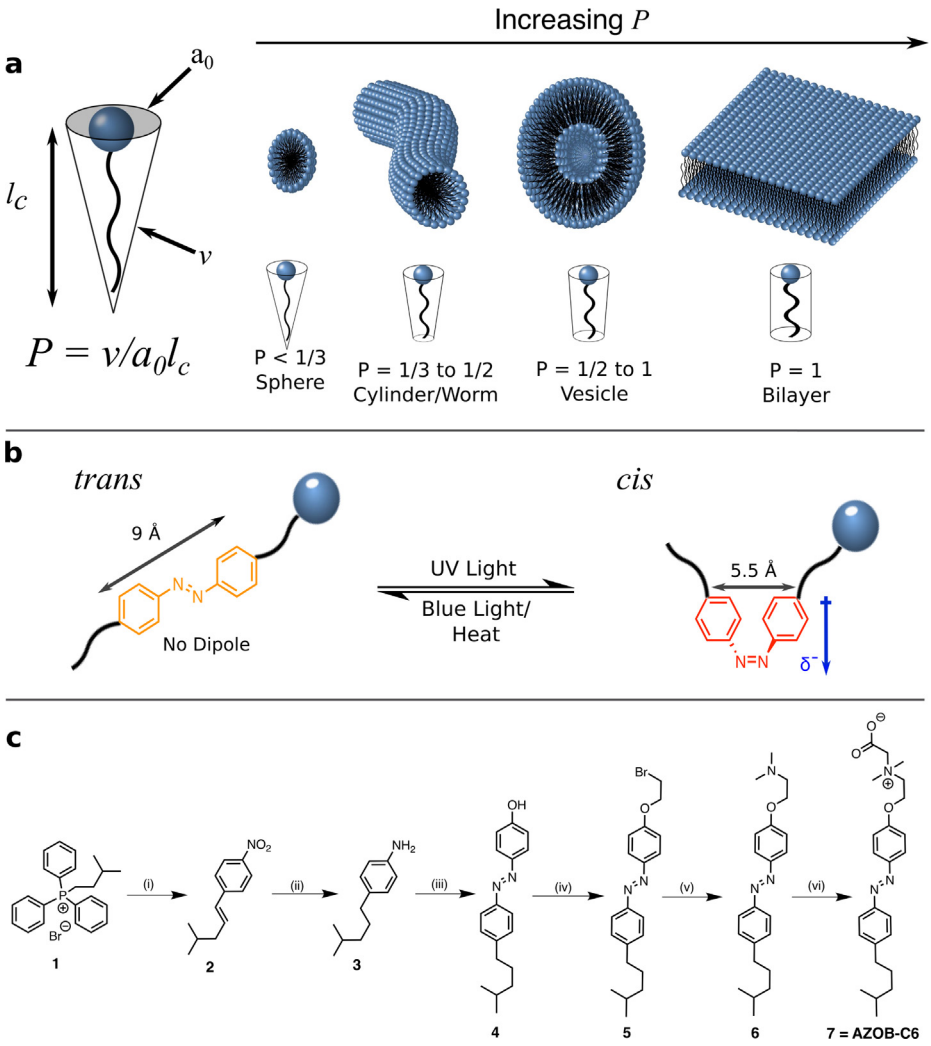


**Fig. 1. a.** Concept of surfactant packing parameter (*P*), with a schematic of various micellar morphologies that can be formed by surfactants. As relative tail group volume increases, lower average curvature structures are favoured. **b.** Photo-switching of a generic azobenzene-containing surfactant showing its influence on molecular geometry and the dipole moment of the *cis* azobenzene isomer. **c.** Scheme for synthesis of azo-surfactant (**7**) from isopentyltriphenylphosphonium bromide (**1**). Triphenylphosphonium **1** was synthesised from commercially available materials as detailed in the material and methods section. Reaction conditions were as follows: (i) *n*-BuLi (0.92 equiv.), 4-nitrobenzaldehyde (0.77 equiv.), THF, −78 °C→0 °C, 4 h, 85%; (ii) 10% wt Pd/C (0.1 equiv. w/w), $H_2$, EtOH, RT, 16 h, quant.; (iii) $NaNO_2$ (1.1 equiv.), $HCl_{(aq.)}$ (37%), phenol (1.0 equiv.) $NaHCO_3$, $H_2O$, 0 °C, 4 h, 84%; (iv) 1,2-dibromoethane (5.0 equiv.), $K_2CO_3$ (3.0 equiv.), ACN, reflux, 48 h, 94%; (v) Dimethylamine (40% in $H_2O$, 10.0 equiv.), $K_2CO_3$ (3.0 equiv.), RT, 72 h, quant.; (vi) Chloroacetic acid (3.0 equiv.), KI (1.0 equiv.), NaOH (1 M in $H_2O$), EtOH, reflux, 24 h, 82%.

and analyse the beam [36]. A neutron wavelength of 4.74 Å was used in these measurements, obtaining a maximum *q*-range of 0.000050.005 Å (0.110 m length scales). USANS data were desmeared using standard procedures to obtain absolute scattering intensity as a function of *q*. Modelling of all data was performed using the software "SasView" (http://www.sasview.org).

*2.2.2. General instrumentation*

Nuclear magnetic resonance spectroscopy was performed using a Bruker DRX400 spectrometer operating at 400 MHz for proton NMR ($^1$H NMR) and 101 MHz for carbon NMR, as solutions in deuterated solvents as specified.

Infrared spectra (IR) were recorded using an Agilent Technologies Cary 630 FTIR.

Pendant drop tensiometry measurements were performed using Opendrop 1.1 open source software [37] with a Flea3 CMOS camera (Point Grey, Richmond, Canada) camera and a custom-built pendant drop setup. Measurements were taken after the droplet had equilibrated for 100 s.

UV–visible (UV-vis) absorption spectra were recorded at room temperature using a Varian Cary 1E UV- vis spectrophotometer. Low concentration measurements were performed with a 10 mm path length cell. High concentration UV–vis spectra were performed as follows: A small drop of the 1% wt solution was sandwiched between two quartz slides and compressed slightly to give a thin film of sample. This was then affixed in the path of the UV–vis instrument and the spectrum recorded.

Melting points were recorded in an ISG melting point apparatus. A Heidolph Laborota 4000 Efficient Rotovap was used for removal of solvents.

Liquid chromatography-mass spectrometry (LC-MS) was performed on an Agilent 1260 Infinity with a 6120 Quadrupole LCMS using a Poroshell 120 column (EC-C18, 3.0 x 50 mm, 2.7 μm) with a flow rate of 0.5 mL per minute.

High-resolution mass spectrometry (APCI, ESI) was conducted on a Thermo Scientific QExactive FT-MS. Positive ion EI mass spectra were obtained using a Thermo Scientific DFS mass spectrometer using an ionisation energy of 70 eV. Accurate mass measurements were obtained with a resolution of 5000–10000 using PFK (perfluorokerosene) as the reference compound.

Rheological measurements were conducted using an Anton Parr MC302 Rheometer using a CP-50 cone and plate geometry with a

570 μL sample volume. The system is equipped with a Peltier plate temperature unit with counter cooling to allow temperature control. Sample measurements were performed at 25 °C. Samples were loaded using a micropipette and allowed to thermally equilibrate before being subject to a pre-shear and relaxation process. Samples were sheared at 100 $s^{-1}$ for 60 s and then allowed to rest for between 5 and 30 min to allow the microstructure to recover before each measurement was performed.

Dynamic light scattering was performed using a Brookhaven NanoBrook Omni in particle sizing mode, using a 640 nm laser with detection at 90° to the incidence.

### 2.3. Synthetic methods and characterisation

#### 2.3.1. Isopentyltriphenylphosphonium bromide (1)

To 3-methyl-1-bromo-butane (2.52 g, 16.7 mmol) and triphenylphosphine (4.38 g, 16.7 mmol) were added toluene (30 mL), stirring to dissolve. The reaction mixture was heated to reflux with stirring for 72 h resulting in a white precipitate. The reaction mixture was then cooled to 0 °C, the precipitate collected by filtration, and then washed with cold toluene (3 × 30 mL), followed by hexanes (2 × 30 mL) to yield the title compound as a white crystalline solid (2.44 g, 97%), Mp 114.3–115.2 °C; $^1$H NMR (400 MHz, $CDCl_3$) $\delta$ 8.13 7.26 (m, 15H), 3.59 3.36 (m, 2H), 1.96 1.71 (m, 1H), 1.36 (p, $J$ = 7.9 Hz, 2H), 0.82 (d, $J$ = 6.6 Hz, 6H); $^{13}$C NMR (101 MHz, $CDCl_3$): $\delta$ 135.0 (d, $J^{C,P}$ = 2.9 Hz), 133.4 (d, $J^{C,P}$ = 10.0 Hz), 130.4 (d, $J^{C,P}$ = 12.4 Hz), 117.9 (d, $J^{C,P}$ = 85.4 Hz), 30.8 (d, $J^{C,P}$ = 4.6 Hz), 28.6 (d, $J^{C,P}$ = 15.8 Hz), 22.0, 21.2, 20.7; IR (ATR): 1437, 1110 $cm^{-1}$; HRMS (m/z): $[M]^+$ calcd. for $C_{23}H_{36}P$, 333.1772; found 333.1774.

#### 2.3.2. (4-Methylpent-1-en-1-yl)-4-nitrobenzene (2)

Isopentyltriphenylphosphonium bromide (8.00 g, 19.37 mmol) was added to dry THF (50 mL) and stirred to form a suspension. The reaction mixture was then cooled to −78 °C and *n*-BuLi (8.88 mL, 2 M in cyclohexane) was added dropwise. Temperature was maintained at −78 °C and the reaction stirred for 30 min before allowing it to warm to room temperature and stirring for a further 30 min. The reaction was then cooled again to −78 °C and a solution of 4-nitrobenzaldehyde (2.44 g, 16.14 mmol) in dry THF (20 mL) was added dropwise with stirring. After addition was complete the reaction mixture was warmed to room temperature and stirred for a further 3 h. Upon completion, the reaction was quenched using sat. $NH_4Cl_{(aq)}$, solvent removed *in vacuo* and the residue re-dissolved in $H_2O$ (30 mL). This was then extracted with DCM (3 × 30 mL), the organic layers washed with $H_2O$ (2 × 30 mL) and brine (30 mL), dried with $MgSO_4$ and the solvent removed *in vacuo*. The residue was then purified by flash column chromatography (3:97 EtOAc/Hexanes, $R_f$ = 0.25) to yield the title compound **2** as an orange oil (2.83 g, 85%) as an isomeric mixture in a 3:1 ratio. $^1$H NMR (400 MHz, $CDCl_3$) $\delta$ 8.19 (d, $J$ = 8.8 Hz, 2H Isomer A), 8.15 (d, $J$ = 8.9 Hz, 2H, Isomer B), 7.46 (d, $J$ = 8.9 Hz, 2H, Isomer B), 7.41 (d, $J$ = 8.4 Hz, 2H, Isomer A), 6.49 (d, $J$ = 11.9 Hz, 1H, Isomer A), 6.41 (m, 1H, Isomer B), 5.89 (dt, $J$ = 11.8, 7.3 Hz, 1H), 2.22 (td, $J$ = 7.1, 1.9 Hz, 2H), 1.75 (m, 1H), 0.96 (d, $J$ = 6.7 Hz, 6H, Isomer B), 0.93 (d, $J$ = 6.7 Hz, 1H, Isomer A); $^{13}$C NMR (101 MHz, $CDCl_3$) $\delta$ 144.6, 136.0, 135.4, 129.4, 127.6, 126.3, 124.0, 123.5, 77.31, 77.0, 76.7, 42.5, 37.7, 30.9, 28.9, 28.5, 22.3; IR (ATR): 2956, 1594, 1512, 1338, 854 $cm^{-1}$; HRMS (m/z): $[M]^-$ calcd. for $C_{12}H_{14}NO_2$, 204.102454; found 204.10563.

#### 2.3.3. 4-(4-Methylpentyl) aniline (3)

Pd/C (280 mg, 10% w/w) and ethanol (30 mL) were combined and stirred to make an even suspension. The mixture was then bubbled with $N_2$ gas for 30 min before addition of 1-(4-methyl pent-1-en-1-yl)-4-nitrobenzene (2.80 g, 13.7 mmol). The reaction vessel was then purged under vacuum and backfilled with $H_2$ gas 3 times before allowing the reaction to stir under a $H_2$ atmosphere for 16 h at room temperature. Upon completion, the reaction mixture was filtered through a pad of Celite and the solvent removed *in vacuo* to yield **3** as a brown oil (2.41 g, quant.); $^1$H NMR (400 MHz, $CDCl_3$) $\delta$ 6.97 (d, $J$ = 5.8 Hz, 2H), 6.62 (d, $J$ = 6.0 Hz, 2H), 3.52 (bs, 2H), 2.48 (t, $J$ = 7.9 Hz, 2H), 1.55 (m, 2H), 1.22 (m, 3H), 0.87 (d, $J$ = 6.6 Hz, 6H); $^{13}$C NMR (101 MHz, $CDCl_3$) $\delta$ 144.1, 133.3, 129.2, 115.4, 77.5, 77.2, 76.8, 38.7, 35.5, 29.8, 28.0, 22.7; IR (ATR): 1619, 1515, 1269 $cm^{-1}$; HRMS (m/z): $[M]^+$ calcd. for $C_{12}H_{20}N$, 178.1596; found 178.1585.

#### 2.3.4. 4-((4-(4-Methylpentyl) phenyl) diazenyl) phenol (4)

4-Isobutylaniline (1.26 g, 7.01 mmol) was dissolved in a mixture of $H_2O$ (14 mL) and conc. HCl (1.8 mL). The reaction mixture was then cooled to 0 °C and a solution of $NaNO_2$ (532 mg, 7.71 mmol) in $H_2O$ (20 mL) was added dropwise. The temperature was maintained and the reaction stirred for 30 min before a solution of phenol (667 mg, 7.01 mmol) in $H_2O$ (20 mL) was added dropwise. This was stirred for a further 1 h then neutralised using $NaHCO_3$(s). After neutralisation, the reaction was warmed to room temperature and stirred for 3 h. Upon completion, the reaction mixture was adjusted to pH the 4 using 1 M $HCl_{(aq)}$ and then extracted with DCM (3 × 50 mL). The combined organics were washed with $H_2O$ (50 mL) followed by brine (50 mL) and then dried using $MgSO_4$. Solvent was removed *in vacuo* and the residue purified by flash column chromatography (1:9 EtOAc/Hexanes, $R_f$ = 0.23) to yield **4** as an orange solid (1.74 g, 88%). $^1$H NMR (400 MHz, $CDCl_3$) $\delta$ 7.86 (d, $J$ = 8.8 Hz, 2H), 7.80 (d, $J$ = 8.3 Hz, 2H), 7.30 (d, $J$ = 8.4 Hz, 2H), 6.94 (d, $J$ = 8.8 Hz, 2H), 5.30 (s, 1H), 2.66 (t, $J$ = 7.7 Hz, 2H), 1.63 (m, 3H), 1.25 (m, 2H), 0.88 (d, $J$ = 6.6 Hz, 6H); $^{13}$C NMR (101 MHz, $CDCl_3$) $\delta$ 158.3, 151.0, 147.3, 146.1, 129.2, 125.0, 122.7, 115.9, 77.5, 77.2, 76.8, 38.7, 36.3, 29.3, 28.0, 22.7; IR (ATR): 2924, 1587, 1248, 834 $cm^{-1}$; HRMS (m/z): $[M]^+$ calcd. for $C_{18}H_{22}N_2O$, 283.1810; found 283.1797.

#### 2.3.5. 1-(4-(2-Bromoethoxy) phenyl)-2-(4-(4-methylpentyl) phenyl) diazene (5)

Compound **4** (309 mg, 1.10 mmol) was added to $CH_3CN$ (30 mL), 1,2-dibromoethane (1.03 g, 5.50 mmol) and $K_2CO_3$ (412 mg, 3.30 mmol). The reaction mixture was heated to reflux with stirring for 48 h. Upon completion the reaction was cooled, filtered, the filtrate solvent removed *in vacuo* and the residue was purified by flash column chromatography (3:97 EtOAc/Hexanes, $R_f$ = 0.18) to yield **5** as a powdery orange solid (402 mg, 94%); $^1$H NMR (400 MHz, $CDCl_3$) $\delta$ 7.90 (d, $J$ = 9.0 Hz, 2H), 7.80 (d, $J$ = 8.4 Hz, 2H), 7.30 (d, $J$ = 8.4 Hz, 2H), 7.02 (d, $J$ = 9.0 Hz, 2H), 4.38 (t, $J$ = 6.3 Hz, 2H), 3.68 (t, $J$ = 6.3 Hz, 2H), 2.66 (t, $J$ = 7.7 Hz, 2H), 1.25 (m, 3H), 0.89 (d, $J$ = 6.6 Hz, 6H); $^{13}$C NMR (101 MHz, $CDCl_3$) $\delta$ 160.3, 151.1, 147.6, 129.2, 124.7, 122.7, 115.0, 38.7, 36.2, 29.3, 28.9, 29.0, 22.7, 18.5; IR (ATR): 1953, 1580, 1235, 849 $cm^{-1}$; HRMS (m/z): $[M]^+$ calcd. for $C_{20}H_{25}BrN_2O$, 389.1228, found 389.1217.

#### 2.3.6. N,N-Dimethyl-2-(4-((4-(4-methylpentyl) phenyl) diazenyl) phenoxy) ethan-1-amine (6)

Compound **5** (402 mg, 1.04 mg) was added to THF (30 mL), dimethylamine (1.17 mL, 40% w/w in $H_2O$) and $K_2CO_3$ (399 mg, 3.12 mmol) and the reaction mixture stirred at RT for 72 h. Upon completion, the reaction mixture was filtered, the filtrate washed with sat. $NaHCO_{3(aq.)}$ (2 × 30 mL), dried over $MgSO_4$ and the solvent removed *in vacuo* to yield **6** as an orange oil (365 mg, quant.); $^1$H NMR (400 MHz, $CDCl_3$) $\delta$ 7.89 (d, $J$ = 8.9 Hz, 2H), 7.80 (d, $J$ = 8.3 Hz, 2H), 7.30 (d, $J$ = 8.3 Hz, 2H), 7.03 (d, $J$ = 8.9 Hz, 2H), 4.16 (t, $J$ = 5.7 Hz, 2H), 2.78 (t, $J$ = 5.7 Hz, 2H), 2.66 (t, J = 7.7 Hz, 2H), 2.37 (s, 6H), 1.65 (m, 3H), 1.26 (m, 2H), 0.88 (d, J = 6.6 Hz, 6H); $^{13}$C NMR (101 MHz, $CDCl_3$) $\delta$ 161.2, 151.2, 147.3, 146.0, 129.2, 124.7, 122.7, 114.9, 66.5, 58.4, 46.1, 38.7, 36.3, 29.3, 28.0, 22.7.;

IR (ATR): 2926, 1598, 1243, 835 $cm^{-1}$; HRMS (m/z): $[M]^+$ calcd. for $C_{22}H_{31}N_3O$, 354.2545; found 354.2516.

#### 2.3.7. 2-(Dimethyl(2-(4-((4-(4-methylpentyl) phenyl) diazenyl) phenoxy) ethyl) ammonio) acetate (7)

Compound **6** (1.00 g, 2.83 mmol) was added to chloroacetic acid (803 mg, 8.499 mmol), potassium iodide (470 mg, 2.83 mmol) and ethanol (30 mL). The reaction mixture was adjusted to pH 10 using 2 M $NaOH_{(aq.)}$ and then heated to reflux with stirring for 24 h. Upon completion, the reaction was neutralised using sat. $NH_4Cl_{(aq.)}$ then cooled to 50 °C and the temperature maintained whilst a stream on nitrogen was blown over to remove solvent (do not subject reaction mixture to vacuum, cavitation will likely occur). The residue was then dissolved in a 95:5 $H_2O/CH_3CN$ mixture, filtered and the filtrate purified by gradient elution reverse phase flash column chromatography (95:5 → 1:9 $H_2O/CH_3CN$) to yield **7** as a yellow solid (949 mg, 82%). $^1H$ NMR (400 MHz, $CDCl_3$): $\delta$ 7.86 (d, $J$ = 8.4 Hz, 2H), 7.77 (d, $J$ = 8.0 Hz, 2H), 7.27 (d, $J$ = 8.2 Hz, 2H), 6.99 (d, $J$ = 9.1 Hz, 2H), 4.86 (bs, 2H), 4.24 (bs, 4.00 2H), 3.42 (s, 6H), 2.63 (s, $J$ = 7.7 Hz, 2H), 1.60 (m, 3H), 1.22 (m, 2H), 0.87 (d, $J$ = 6.6 Hz, 6H); $^{13}C$ NMR (101 MHz, $CDCl_3$) $\delta$ 159.1, 151.0, 148.0, 146.4, 129.2, 126.4, 124.9, 122.8, 114.9, 77.5, 77.2, 76.8, 62.8, 62.6, 53.1, 38.7, 36.2, 29.3, 28.0, 22.7; IR (ATR): 2960, 1625, 1243, 837 $cm^{-1}$; HRMS (m/z): $[M]^+$ calcd. for $C_{24}H_{33}N_3O_3$, 412.2600; found 412.2573.

## 3. Results and discussion

### 3.1. Molecular design elements for a single-component PRF

Much of the work in the field of surfactant research has sought to establish structure-performance relationships, *i.e.* the complex and subtle ways that molecular architecture influences surfactant aggregation. From these relationships, we designed a molecule incorporating structural motifs to promote WLM formation and allow effective photo-switching of aggregate morphology, with the intent of realizing a single component PRF. It has been shown that the extent to which azobenzene photo-switching controls packing parameter of azo-surfactants relates inversely to the length of the alkyl tail-group and the length of the spacer between the azobenzene and the head group [38]. Therefore, to maximise the influence that the azobenzene photo-switch has on aggregate morphology, surfactants should have a compact molecular structure, avoiding the inclusion of extended, flexible alkyl chains. Ionic surfactant head groups are more compact than their non-ionic counterparts and provide greater solubility [39], however, charge repulsion between the head groups can provide a barrier for formation of low curvature aggregate structures [40]. Betaines, a class of zwitterionic head group, maintain the localised charge density of other ionic functionalities but generate surfactants capable of forming WLMs without the need for charge-screening additives [41,42]. These properties, alongside their environmentally benign nature [43,44], make them an ideal head group for development of a single-component PRF surfactant. Inducing assembly into WLMs also requires sufficient steric bulk in the tail group [19], a goal usually achieved by lengthening of the surfactants alkyl tail, though this may come at the cost of limiting solubility [45–47] and reducing efficacy of the azobenzene photo-switch. We instead opted to incorporate branching into the tail group, in the form of a 4-methylpentyl (*iso*-C6) functionality, to increase packing parameter without compromising the photo-switching functionality. The resulting molecular structure, AZOB-C6 (**7**), was synthesized *via* the scheme shown in Fig. 1c.

### 3.2. Interfacial and UV–vis spectral properties of the AZOB-C6 molecule

The effect of AZOB-C6 (**7**) on interfacial tension was measured as a function of concentration using pendant drop tensiometry (Fig. 2a). Equilibrium interfacial tensions ($\gamma_{eq}$) of 33.2 $mN{\cdot}m^{-2}$ and 31.6 $mN{\cdot}m^{-2}$ were found for the *cis* and *trans* isomers respectively. CMCs were found at 0.13 mM (*trans*) and 0.40 mM (*cis*). Using the Gibbs isotherm area occupied at the interface was calculated to be 15 $Å^2$ for the *trans* isomer and 31 $Å^2$ for the *cis* isomer. The marked change in area occupied at the interface upon isomerization of AZOB-C6 (**7**) shows it's potential to be used for the generation of photo-controlled aggregates.

To more deeply probe the photo-isomerization of AZOB-C6 (**7**), UV–vis spectra of a 0.01 mM solution were obtained before (*trans* isomer) and after (*cis* isomer) irradiation with UV light (Fig. 2b). The *trans*→*cis* and *cis*→*trans* isomerizations were performed by irradiation with 365 nm and 470 nm light sources respectively. Previous studies indicate that *trans* azo-surfactants can exhibit $\pi$-$\pi$ interactions when in self-assembelies [48,49]. The nature of these interactions can be inferred from changes in UV–vis absorbance spectrum at concentrations above the critical micelle concentration. To investigate the role of $\pi$-$\pi$ interactions in self-assembly of AZOB-C6 **(7)**, a third UV–vis measurement was performed, using a 24 mM (1 wt%) solution of the *trans* isomer. It can be seen that the $\pi \rightarrow \pi^*$ transition peak in the 300–400 nm region of the spectrum blue-shifts with increasing concentration, from $\lambda_{max}$ = 346 nm to $\lambda_{max}$ = 333 nm for the 0.01 mM and 24 mM samples respectively (Fig. 2b), indicating the presence of H-type (face-to-face) $\pi$-$\pi$ interactions in the self-assembled micelle structure [50]. The $\Delta_{\lambda max}$ of the blue-shift is proportional to the number of azobenzene units in the aggregate, and is distinct for each unique aggregate environment [51]. Given this, the observed asymmetry in the peak at $\lambda_{max}$ = 333 nm in our 24 mM spectrum suggests the presence of multiple overlapping absorption bands combining to give the observed spectral peak shape. In order to deconvolute the 24 mM spectrum and determine $\lambda_{max}$ of the absorbance arising from $\pi$-$\pi$ stacking we combined a fit for the $\pi \rightarrow \pi^*$ transition peak in the 0.01 mM spectrum with a second blue shifted peak to account for the $\pi$-$\pi$ contribution. Fitting was performed using a Guassian function for the 0.01 mM spectrum and a Lorentzian for the $\pi$-$\pi$ contribution peak in the 1% wt spectrum, as these two fits account for the greater mobility of the solution state molecules compared to the aggregated molecules [52,53]. The peak at $\lambda_{max}$ = 333 nm was found to comprise a combination of the monomeric azobenzene $\pi \rightarrow \pi^*$ absorption band from the 0.01 mM solution (Fig. 2c) in combination with a second band centred at 331 nm (Fig. 2d), which we attribute to portion of the azobenzene experiencing $\pi$-$\pi$ interactions.

Most literature accounts of azobenzene H-aggregation report $\lambda_{max}$ values of 300–315 nm for the $\pi \rightarrow \pi^*$ transition in an extended aggregates of chromophores, with higher $\lambda_{max}$ values indicating aggregates of fewer azobenzene units, such as dimers and trimers [48]. The $\lambda_{max}$ = 331 nm $\pi$-$\pi$ stacking contribution in the 24 mM spectrum suggests the presence of trimers, however, these usually only occur in either molecular solutions or mixed surfactant systems, wherein inhomogeneous distribution can allow small clusters of azobenzene to form within the aggregates. As our system comprises only azo-surfactant it is unlikely that the absorbance at $\lambda_{max}$ = 331 nm can be attributed to this phenomenon. Kunitake et al. reported that whilst tightly packed azobenzene bilayers gave $\pi \rightarrow \pi^*$ $\lambda_{max}$ values in the 300–315 nm range, formation of a more fluid bilayer structure caused the $\lambda_{max}$ to shift into the 330–340 nm range [49]. This shift was attributed to more variation in orientation and looser packing of the molecules, thereby resulting a lesser

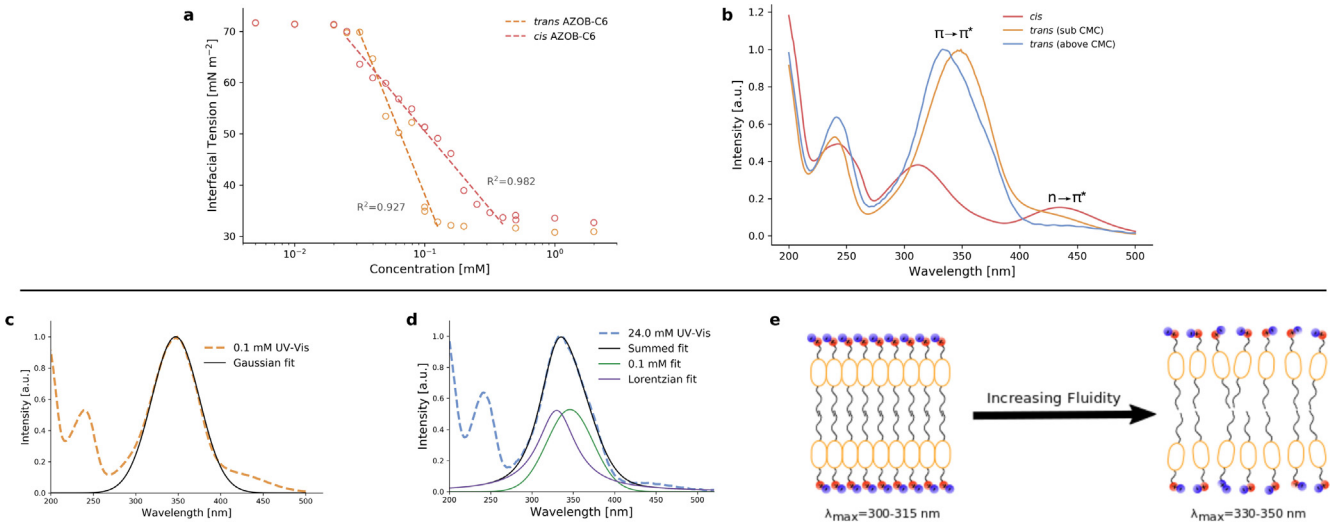


**Fig. 2. a.** Interfacial tension vs concentration plot for *trans* and *cis* isomers of AZOB-C6 (**7**) obtained using pendant drop tensiometry. Gibbs isotherm fits use to obtain area per molecule are shown. $IFT_{trans} = 27.4 \cdot ln(C) - 24.9$ and $IFT_{cis} = 13.2 \cdot ln(C) - 20.2$. b. UV–vis spectra for the *trans* and *cis* isomers of AZOB-C6 (**7**) at 0.01 mM and the *trans* isomer at 24 mM (1 wt%). Electronic transitions corresponding to the absorbance maxima are labelled. Intensity of the spectra has been normalised for ease of comparison. **c.** UV–vis spectrum of the *trans* isomer of AZOB-C6 (**7**) as a 0.01 mM solution with a Gaussian fit ($\lambda_{max}$ = 346 nm) for the $\pi \rightarrow \pi^*$ absorbance peak overlaid. **d.** UV–vis spectrum of the *trans* isomer of AZOB-C6 (**7**) as a 1 wt% solution with a Gaussian fit ($\lambda_{max}$ = 346 nm), Lorentzian fit ($\lambda_{max}$ = 331 nm) and the summed pseudo-Voigt fit ($\lambda_{max}$ = 333 nm) for the $\pi \rightarrow \pi^*$ absorbance peak overlaid. Full fitting parameters are detailed in ESI (Table S1). **e.** Schematic showing the structural and packing changes between a more crystalline (left) and more fluid (right) azo-surfactant bilayer assembly and the corresponding $\lambda_{max}$ of the azobenzene $\pi \rightarrow \pi^*$ transition.

blue shift (Fig. 2e). We hypothesise that a similar loose $\pi$-$\pi$ interaction is occurring within the micelles formed by AZOB-C6 (**7**). Asymmetry of the 24 mM spectral peak, and significant contribution of the monomeric absorbance band, indicate that a significant portion of the azobenzene surfactants are participating in little or no $\pi$-$\pi$ stacking, prompting our further investigation of the aggregate morphology.

### 3.3. Aggregate characterisation using neutron scattering

Neutron scattering techniques provide a facile and non-destructive method for probing the nano- and micro-structure of surfactant formulations in order to accurately characterize the morphology of the micellar aggregates formed. Small-angle and ultra-small-angle neutron scattering (SANS and USANS) measurements were performed on 15 mM solutions of AZOB-C6 (**7**) in its *trans* and *cis* isomeric states. Fitting the combined SANS and USANS patterns (Fig. 3a) it was found that at 15 mM the *trans* isomer of AZOB-C6 (**7**) self-assembles into WLMs, with a length $\geqslant$1 μm and an elliptical cross section with a minor radius and radial ratio of 22 Å and 1:1.4, respectively. After irradiation with UV light, the measured scattering pattern indicates the presence of ellipsoidal micelles, with a major and minor radius of 38 Å and 17 Å, respectively. The minor radius of both aggregates correlates well with the expected molecular length of *trans* and *cis* isomers (ESI Fig. S3), further supporting the proposed aggregate geometries. It should be noted that the upturn in intensity at low-*q* in the data for the *cis* isomer is not fit by the chosen ellipsoidal model. This upturn is characteristic of the formation of larger fractal cluster structures, caused by weakly attractive intermicellar interactions, and has been observed in other azo-surfactant systems [31,54]. Due to the difficulty in quantifying this phenomenon, an additional fit component was not added to describe it, though this could potentially be achieved by using a mass fractal model. The elliptical cross section of the WLMs of *trans*-AZOB-C6 (**7**) indicates multiple favorable radii of curvature in the cross section, likely caused by $\pi$-$\pi$ interactions between the azobenzene units of the surfactants. Ellipsoidal aggregates have previously been observed in the solution state self-assemblies of other aromatic units [55], and were also attributed to the directional nature of $\pi$-$\pi$ interactions inducing multiple favourable radii of curvature within the self-assembly structure. In the WLM core, $\pi$-$\pi$ interactions would occur concurrently with steric interactions, resulting in sections of $\pi$-$\pi$ dominated and sections of steric driven curvature. This would cause elongation along the axis of the $\pi$-$\pi$ interactions (Fig. 3c) and result in the observed ellipsoid cross section. This would also explain the smaller than expected blue-shift in the UV–vis spectrum compared to that expected for fully H-aggregated azobenzene [56].

The smaller, less ordered and more spherical structure of the *cis*-AZOB-C6 (**7**) aggregates is somewhat counterintuitive if one solely considers the sterics of the two isomers, as the bulkier *cis* isomer should result in a larger packing parameter and therefore larger aggregates with a flatter curvature. We hypothesise that the disruption of the *trans*-azobenzene $\pi$-$\pi$ aggregates and the introduction of a dipole in the tail group upon isomerisation of AZOB-C6 (**7**) molecule from *trans* to *cis* are the primary drivers of the observed change in micellar morphology, rather than pure sterics. In a study on the influence of segmented tail group hydrophobicity, Menger and Galloway found that inclusion of even mildly polar functionality into the tail group of a surfactant could induce formation of small, loose, more globular aggregates than those of a purely hydrophobic alkyl chain counterpart [57]. We believe that the dipole of the *cis* azobenzene isomer has a similar effect in our system, causing a semi-polar intermediate region in the micelle core; this would result in greater penetration of water into the micellar core, thereby causing weaker aggregation and resulting in the looser, less ordered aggregates that are seen after UV irradiation (Fig. 3d) Formation of less densely packed aggregates would also increase the total aggregate volume for *cis*-AZOB-C6 (**7**) compared to its *trans* isomer, which may explain why intermicellar interactions are observed in the SANS pattern of the *cis* isomer but not the *trans* isomer.

Incorporation of additives, such as hydrophobic salts, into surfactant formulations is a common method for tuning self-assembly properties, in particular to induce formation or growth of WLMs. Screening of electrostatic repulsion by salt can allow

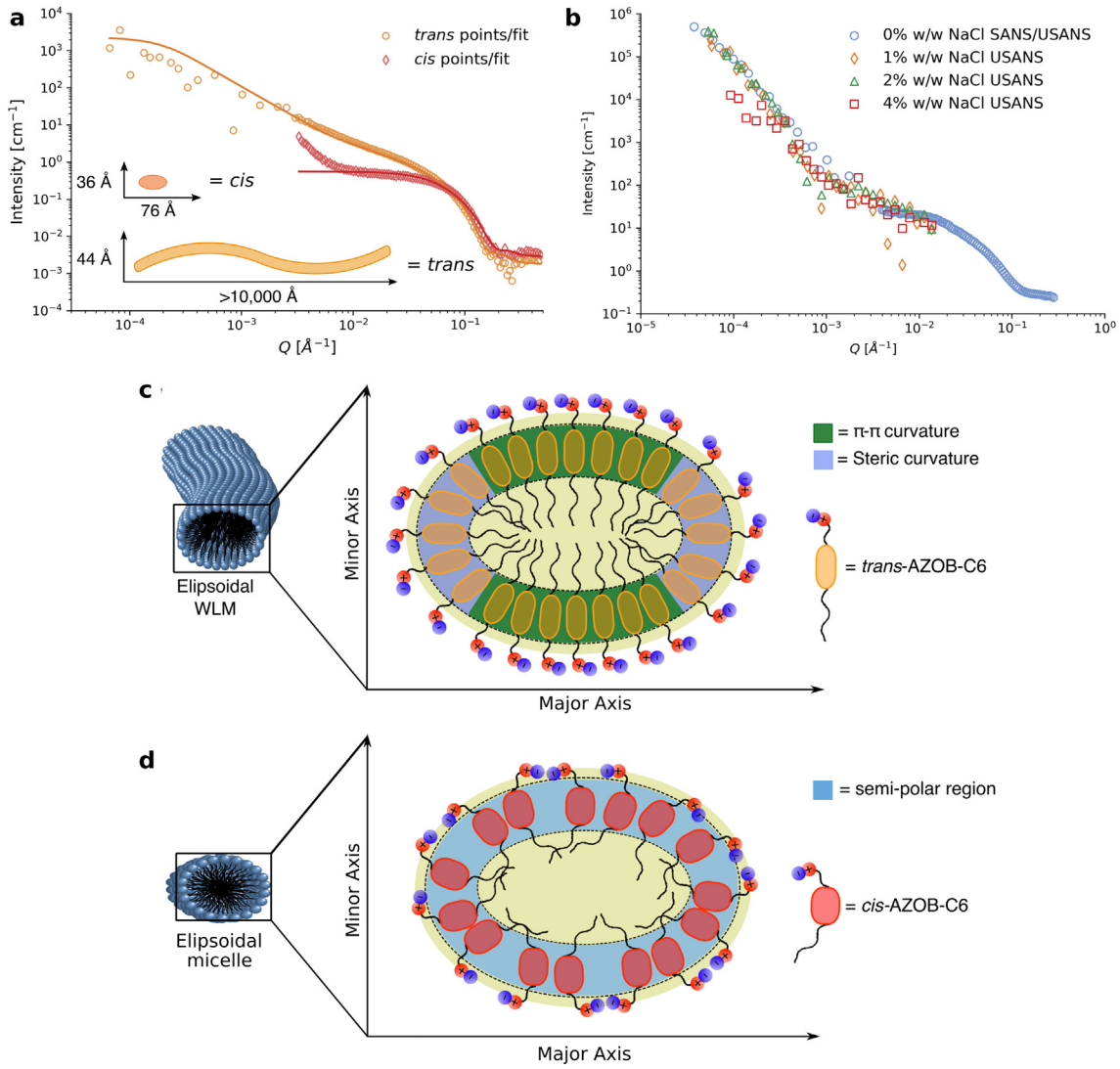


**Fig. 3. a.** Reduced 1D neutron scattering data for 15 mM solutions of AZOB-C6 (**7**) in its *cis* (SANS only) and *trans* (SANS and USANS) isomers in $D_2O$ (hollow points) with model fits and fitting parameters generated from the fits (solid lines). Full fitting parameters and residuals are presented in ESI Table. S2 and Fig. S2 respectively. **b.** USANS patterns for 1 wt% (24 mM) surfactant AZOB-C6 (**7**) in $D_2O$ with increasing concentrations of NaCl. Note that the scattering pattern for the 1% w/w formulation without salt appears different to that of the 15 mM solution as inter-micellar interactions contribute to the scattering pattern at this higher concentration. **c.** Schematic cross section of the elliptical WLMs formed by *trans*-AZOB-C6 (**7**) showing sections of steric and sections of $\pi$-$\pi$ driven curvature that drive the elliptical cross section. **d.** Schematic cross section of the ellipsoidal micelles formed by *cis*-AZOB-C6 (**7**) showing looser, less ordered aggregate structure and semi-polar intermediate region.

charged surfactant head groups to pack more closely, increasing packing parameter, decreasing net curvature and leading to more elongated aggregates. This phenomenon has been observed in alkyl tailed betaine surfactant systems, which elongate and network on addition of NaCl [58]. This prompted us to study the influence of NaCl on our system, using USANS, to detect changes in contour length and network structure which manifest at length scales > 200 nm. NaCl, in amounts from 0 to 4 wt%, was added to 24 mM solutions of surfactant AZOB-C6 (**7**) in its *trans*-dominated photostationary state and the scattering patterns collected (Fig. 3b, 0 wt% SANS and USANS, 1–4 wt% USANS only). Surprisingly, addition of NaCl to 24 mM solutions AZOB-C6 (**7**) resulted in negligible deviation in the USANS region, indicating a WLM network that is insensitive to the addition of salt. This is in contrast to previous observations for alkyl betaine surfactants, and suggests that the self-assembly and long range structuring of AZOB-C6 (**7**) WLMs is not influenced by any electrostatic screening effects of the NaCl. As we have shown, there are significant $\pi$-$\pi$ interactions between azobenzene units in the core of AZOB-C6 (**7**) WLMs. It is possible that these interactions, rather than interactions between head groups, are providing the primary driving force directing the aggregation morphology of AZOB-C6 (**7**). This would explain the insensitivity of the WLM structure to addition of NaCl, as hydrophilic salt ions are unable to penetrate into the micellar core. This hypothesis is in agreement with our observation of and justification for the ellipsoidal cross-section of the AZOB-C6 (**7**) WLMs.

### 3.4. Rheological behaviour of AZOB-C6 solutions

When subjected to UV or blue light, solutions of AZOB-C6 (**7**) undergo a significant change in apparent viscosity, with a 10 wt% (243 mM) solution switching from a thick, orange gel-like material to a slightly viscous, free-flowing red liquid (Fig. 4a, ESI video) To further explore this photo-rheological response, steady-shear viscosity curves of solutions of AZOB-C6 (**7**) at various concentrations in water were obtained before and after irradiation with UV light (Fig. 4b). For solutions of the *trans* isomer, all concentrations were shear thinning, with a shear-independent viscosity region at low

shear rates. At concentrations ⩾2.5 wt% (61 mM) of the *trans* isomer, zero-shear viscosity ($\eta_0$) scales with concentration, following a power law relationship with an exponent of 5.69 (Fig. 4c). A power law relationship between $\eta_0$ and surfactant concentration is expected for an entangled WLM system, and has both been predicted theoretically and confirmed experimentally [59,60]. Deviation from this relationship at 1% w/w (24 mM) indicates a lack of entanglement in this sample, and therefore defines a critical overlap concentration ($C^*$) between 1 and 2.5 wt% for surfactant AZOB-C6 (**7**) in water.

Upon irradiation with UV light, samples ⩽7.5 wt% switched from a viscous shear thinning fluid to a thin, water-like, Newtonian fluid (Fig. 4b). These samples displayed negligible shear thinning across the measured shear rate range, and $\eta_0$ values within one order of magnitude of that of water (0.89 mP·a). At these concentrations the *cis* isomer displayed a linear relationship between surfactant concentration and $\eta_0$ (Fig. 4c), indicating the presence of discrete micelles with little or no morphological change over this concentration range [61]. The 10 wt% sample for the *cis* isomer showed a higher $\eta_0$, likely caused by a concentration-induced elongation of aggregate morphology from small ellipsoids to rodlike micelles, that could align somewhat under shear. This is supported by slight shear thinning (observable at 100–1000 $s^{-1}$) in the viscosity curve for this sample.

Small amplitude oscillatory shear (SAOS) measurements are presented as plots showing elastic modulus ($G'$) and viscous modulus ($G''$) as functions of either oscillation amplitude or oscillation frequency ($\omega$). Controlled amplitude sweep results for the 7.5 wt% *trans* sample (Fig. 4d) display classic viscoelastic response, with $G' > G''$ at lower amplitudes, a crossover/flow point after which shear thinning occurs, and an elastic $G''$ dominated response at higher amplitudes. As expected for a viscoelastic material, the frequency sweep is $G''$-dominated at low $\omega$ and $G'$-dominated at higher $\omega$ (Fig. 4e). Upon isomerization of the 7.5 wt% sample from *trans* to *cis*, the response reverts to viscous-dominated for the entire measured range of amplitudes and frequencies (Fig. 4d–e). Modelling frequency sweep data with Maxwell and Rouse models was attempted, however, the fits obtained were poor. Fitting details and full plots are detailed in the ESI.

### 3.5. Micro-structural response to flow

Rheology coupled SANS measurements were conducted to further investigate the micro-structural response of our WLMs to shearing (flow). By analysing the 2D SANS patterns directionally with respect to the axis of flow, we can observe micro-structural rearrangements that occur when the sample is sheared, and relate these to macro-scale physical properties of the system. Our experiments used a rotational viscometer with a Searle geometry, passing the neutron beam through the centre of a cup and bob perpendicular to the direction of shear (Fig. 5a). The reference frame for analysis is defined with respect to the rotational axis of the rheometer bob as shown in Fig. 5a, with 90° being the direction of flow and 0° the direction of vorticity. All measurements were performed on a 24 mM (1 wt%) solution of surfactant AZOB-C6 (**7**) in $D_2O$ at shear rates between $\dot{\gamma}$ = 0 $s^{-1}$ and $\dot{\gamma}$ = 1200 $s^{-1}$. Shear-induced anisotropy in the collected scattering patterns was analyzed using both sector and annular analyses (Fig. 5b).

Sector analysis averages the scattering intensity as a function of $q$ within a reduced angular sector to give a conventional 1D scattering pattern (Fig. 5c). By comparing the obtained scattering patterns parallel (90°) and perpendicular (0°) to the direction of flow for a given shear rate, we can observe the degree of anisotropy in the system and compare the form factor in and perpendicular to the direction of flow. For our analysis, sectors of $\pi/20$ radians were taken in each direction as this provided the best balance of directionally resolved information and sufficient signal-to-noise. As can be seen in Fig. 5c, scattering patterns collected along flow and vorticity directions for the ($\dot{\gamma}$ = 10 $s^{-1}$) sample are virtually identical, and both match the spectra taken for the the same sample using a conventional static SANS cell. Upon applying shear to the system, we see an increase in scattering intensity along the vorticity direction, and a corresponding decrease in intensity in the direction of flow, which scale with shear rate. This has been previously observed in the SANS of rodlike micelles under shear by Takeda et al. [62] and for WLMs by Kelleppan et al. [42], and indicates alignment of the micelles with the direction of flow.

Comparing the *extent* of alignment with respect to shear rate is most easily accomplished via annular analysis, whereby average scattering intensity from an annulus of specific $q$-range is plotted

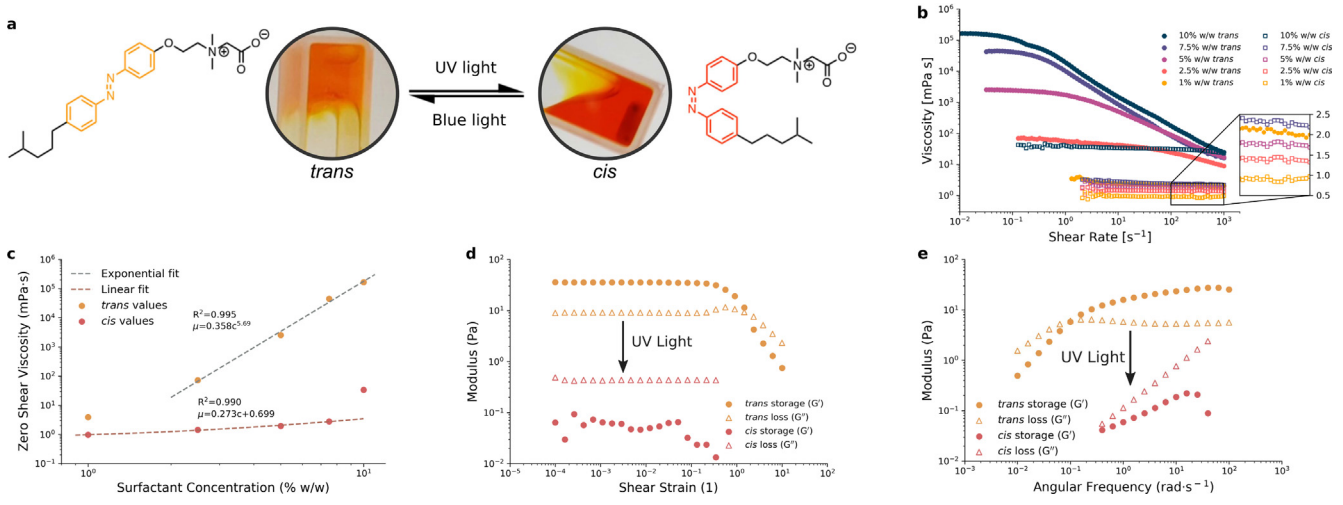


**Fig. 4. a.** Steady shear viscosity data, showing viscosity ($\eta$) as a function of shear rate ($\dot{\gamma}$) for various concentration of AZOB-C6 in water, both as its *trans* and *cis*-dominated photo-stationary states, showing the drop in $\eta_0$ and loss of shear thinning properties upon isomerisation form *trans* to *cis*. Inset uses linear y-scale for clarity. **b.** Plot of $\eta_0$ as a function of surfactant concentration for the *cis* and *trans* isomers of AZOB-C6 (**7**) in solution, with exponential (*trans*) and linear (*cis*) fits as appropriate. **c.** Amplitude sweep for a 10 wt% solution of AZOB-C6 in its *cis* and trans isomers showing a linear viscoelastic region up to 0.133 and a flow point at approximately 1.47 in the *trans* isomer and reversion upon isomerization to a loss dominated material over all measured strains. **d.** Amplitude sweep data for a 10 wt% solution of AZOB-C6 (**7**) before and after UV irradiation. **e.** Frequency sweep data for a 10 wt% solution of AZOB-C6 (**7**) before and after UV irradiation.

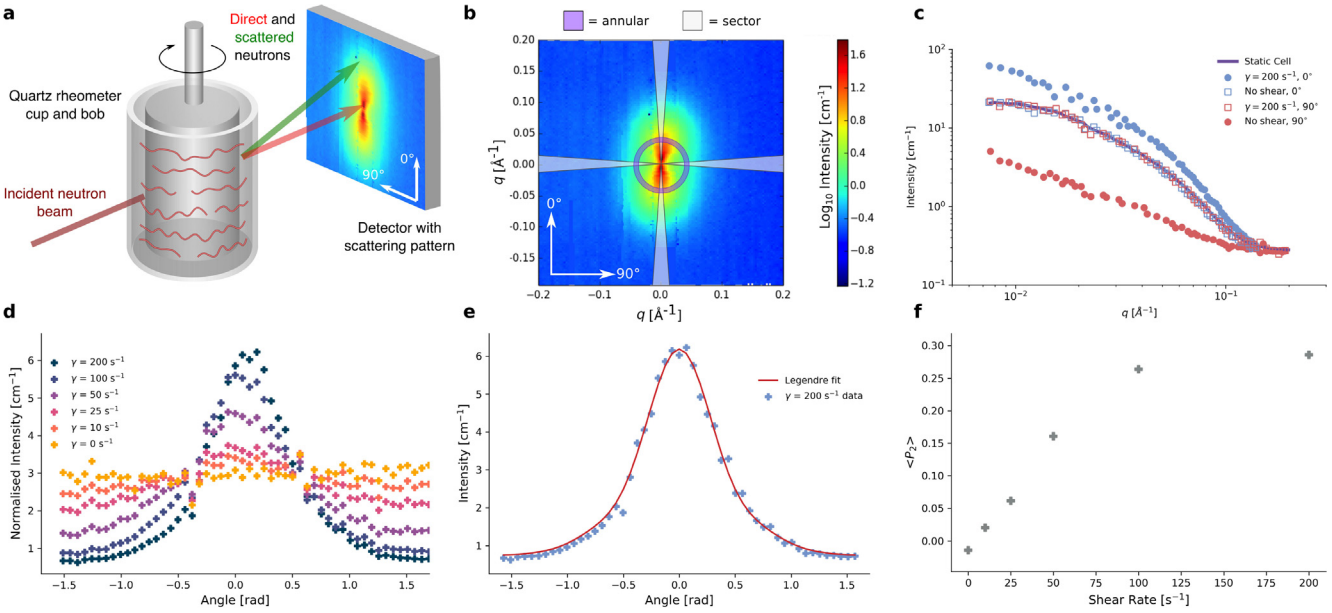


**Fig. 5.** **a.** Schematic of the rheo-SANS setup used for our experiments, showing neutron path as red (direct) and green (scattered) arrows and a sample detector image with directions of analysis indicated. **b.** Example 2D scattering pattern with sections taken for annular and radial analysis shown. **c.** Reduced 1D data for sectors take in the directions of vorticity (90°) and flow (0°) for $\dot{\gamma}$ = 0 $s^{-1}$ and $\dot{\gamma}$ = 200 $s^{-1}$. Static SANS data is shown in purple. Plots of the remaining shear rates are provided in the ESI (ESI Fig. S5) **d.** Reduced 1D data for annular sections taken from the 2D scattering patterns from $\dot{\gamma}$ = 0 $s^{-1}$ to $\dot{\gamma}$ = 200 $s^{-1}$. Data from only −1.5 to 1.7 radians is presented for clarity. Full plots and the remaining shear rates are provided in the ESI (ESI Fig. S6). **e.** Plot of the $\dot{\gamma}$ = 200 $s^{-1}$ annular data with Legendre polynomial fit overlaid. Fits for the remaining shear rates are presented in the ESI (ESI Fig. S7).**f.** Plot of Hermans' orientation parameter ($\langle P_2 \rangle$) vs shear rate over the range $\dot{\gamma}$ = 0 $s^{-1}$ to $\dot{\gamma}$ = 200 $s^{-1}$.

as a function of angle around the centroid of the scattering pattern. This allows us to observe anisotropy developing as a peak in intensity in the direction of vorticity (0°), with a corresponding drop in intensity in the direction of flow. Our analysis was performed using an annular section from $q$ = 0.04–0.06 $Å^{-1}$, as this region showed significant anisotropy in the sector analysis (Fig. 5c) while avoiding the areas of higher noise at low-$q$. Collected data display the expected increase in scattering intensity in vorticity and decreases in flow directions as shear rate increases, indicating a concomitant increase in micelle alignment (Fig. 5d) [62]. The most robust method for quantification of alignment using annular rheo-SANS data is by derivation of a Hermans' orientation parameter ($\langle P_2 \rangle$), which ranges from 0, representing a completely random anisotropic system, to 1, representing a system with perfect parallel alignment [63]. This method is widely used to quantify alignment of polymers and other fibrous or elongated anisotropic particle systems [64–66]. Annular data from $-\frac{\pi}{2}$ to $\frac{\pi}{2}$ radians were fit using a Legendre polynomial, an example of which is shown in Fig. 5e, with remaining fits presented in the ESI (ESI Fig. S7). From these fits, the Hermans' orientation parameters were calculated and plotted as a function of shear rate (Fig. 5f), displaying a linear increase in alignment from $\dot{\gamma}$ = 0 $s^{-1}$ to $\dot{\gamma}$ = 100 $s^{-1}$. Interestingly, onset of alignment is seen at the lowest shear rate to which our sample was subjected ($\dot{\gamma}$ = 10 $s^{-1}$), which is significantly earlier than previously observed for other betaine-based WLM systems, where the onset of anisotropy occurs at shear rates greater than $\dot{\gamma}$ = 100 $s^{-1}$ [42]. Literature accounts of the $\langle P_2 \rangle$ values for WLM systems similar to the one presented here are sparse, however, Arenas-Gómez et al. observed a comparable $\langle P_2 \rangle$ value (≈ 0.35 at $\dot{\gamma}$ = 100 $s^{-1}$) for a 71.3 mM mixed zwitterionic/anionic surfactant system [67]. The similar $\langle P_2 \rangle$ value for our system is surprising in this case, as our surfactant was measured at a far lower concentration (24 mM), which usually results in lower micellar alignment for a given shear rate.

The ability for AZOB-C6 (**7**) WLMs to align at such strikingly low shear rates and concentration indicates a relatively greater rigidity of the micelles when compared to assemblies of simple *n*-alkyl tailed surfactants, as ease of alignment under flow can been directly linked to the rigidity of the colloidal particles in question. Additionally, higher micellar rigidity inhibits reptation, and can therefore increase the proportional elastic response of the material [41]. Greater rigidity of the AZOB-C6 (**7**) micelles further supports the idea that $\pi$-$\pi$ interactions between the azobenzene tail groups significantly affect aggregation structure, as these interactions have a greater strength and degree of directionality than hydrophobic interactions alone, contributing to formation of more rigid micelles. One could envision this design principle being used to design surfactant molecules that produce more elastic WLM networks, bridging the gap between dynamic, shear responsive viscoelastic fluids and elastic, non-responsive gels, via the inclusion of aromatic units within conventional surfactant structures.

### 3.6. Application in the control of particle diffusion rate

One of the proposed applications for fluids with stimulus-responsive rheological properties is use as dispersion media to control the diffusion of macromolecules or particles. Systems of this kind have relevance in many fields as they can modulate reaction rates [68,69], operate in drug delivery systems [70], control bio-separations [71,72] and allow study of protein diffusion. To show that our photo-rheological fluid formulation could be used in this role, we performed dynamic light scattering (DLS) measurements to determine the relative diffusion rates ($D_t$) of particles in the system both before and after isomerisation of the AZOB-C6 (**7**) molecule. DLS was chosen as the time-dependent correlation measurements it performs directly render diffusion rates. Fitting the obtained autocorrelation functions using a single exponential decay allows calculation of the diffusion coefficients ($D_t$) for particles in the system. It is worth noting that the Stokes–Einstein equation used to obtain diffusion coefficient from the correlation function assumes the medium is Newtonian in nature, i.e. its viscosity is a fixed value and is independent of any shear applied.

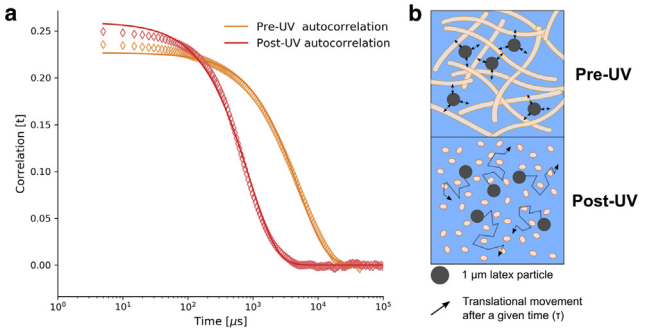


**Fig. 6. a.** Autocorrelation functions with single exponential fits for 1 μm particles in a 2.5 wt% solution of AZOB-C6 (**7**) in water before and after irradiation with UV light for 3 h. Apparent $D_t$ values of $2.0\times10^{-4}$ and $1.1\times10^{-3}$ were calculated for the pre and post-UV samples, respectively. **b.** Schematic showing particles with translational diffusion restricted by an entangled WLM network (left, pre-UV) and particles with unrestricted diffusion in a system of ellipsoidal micelles (right, post-UV irradiation).

As we have shown, solutions of the *trans* isomer of AZOB-C6 (**7**) form WLMs that cause non-Newtonian flow properties. Because of this, the assumptions of the Stokes–Einstein equation are not met and an experimentally precise translational diffusion coefficient cannot be derived using this method. We can however use this method to derive an *apparent* transitional diffusion coefficient that can be used to make qualitative comparisons between the two isomers in solution.

Measurements were performed by adding 1 μm diameter latex particles (0.1 wt%) to a 2.5 wt% solution of AZOB-C6 (**7**) in water. DLS measurements of the sample were then performed in the *trans*-dominated photo-stationary state and again after irradiation with UV light for 3 h. Fitted autocorrelation functions provided $D_t$ values of $4.10\times10^{-13}$ and $2.34\times10^{-12}$ $m^2{\cdot}s^{-1}$ for the pre and post-UV measurements respectively, indicating a fivefold increase in particle mobility after UV irradiation of the sample (Fig. 6). This fivefold change in diffusion contrasts the larger, approximately fifty fold, change in $\eta_0$ between the *cis* and *trans* isomers of AZOB-C6 (**7**) as a 2.5 wt% solution. The disparity between these two measurements could be attributed to the aforementioned limitations in using the Stokes–Einstein equation for a non-Newtonian fluid. However, it is also plausible that the presence of latex particles could influence the micellar micro-structure. Incorporation of smaller nano-particles into WLM networks has been studied previously, with particles causing increased viscosity via formation of junctions that increase the degree of networking [73–75]. Due to the significantly larger size of our latex particles (1 μm diameter vs >100 nm), while we would expect particle–micelle interactions to occur, we would not presume the same mode of interaction in our system as observed in other studies. These preliminary DLS experiments show the potential for AZOB-C6 (**7**), and PRFs more generally, to be used in the mediation of particle diffusion. However, further study of the influence of various particles will be required for optimisation of such systems, along with more advanced particle tracking techniques to correctly separate diffusional and viscoelastic contributions to particle motion.

## 4. Conclusions

We have applied rational molecular design to obtain a surfactant molecule capable of forming highly effective photo-rheological fluids (PRFs) as a single-component in water. Incorporation of and azobenzene functionality into the molecule has allowed for light induced control over aggregation morphology and the bulk flow properties of the formulations. SANS analysis shows that AZOB-C6 (**7**) is capable of forming light-responsive wormlike micelles that assemble or disaggregate on application of an appropriate light based trigger. This reversible photo-control of the nanostructure allows control of $\eta_0$ over a range of 4 orders of magnitude and switching from a viscoelastic fluid to an entirely viscous dominated liquid across the entire frequency range of our small amplitude oscillatory shear measurments. Study of aggregation structures using UV–vis and rheo-SANS revealed that the *trans* azobenzene functionalities of AZOB-C6 (**7**) undergo $\pi$-$\pi$ interactions when aggregated into micelles. These interactions play a pivotal role in determining the packing properties of the molecule, and in turn influence the micellar nanostructure causing the elongation and rigidification of the aggregates, as demonstrated by their ease of alignment under shear. Finally, the applicability and efficacy of AZOB-C6 (**7**) in modulating particle diffusion was shown using DLS experiments. This molecule represents the first rationally designed single component photo-rheological fluid, the study of which has revealed the influence of $\pi$-$\pi$ interactions on surfactant aggregation behaviour. The insights into azo-surfactant aggregation derived from the study of this molecule could inform development of new molecules that exploit $\pi$-$\pi$ interactions as a method for tuning surfactant self-assembly properties, giving access to new diverse self-assembly structures with desirable functionality.

## CRediT authorship contribution statement

**C.S.G.B.:** Conceptualization, Data curation, Formal analysis, Investigation, Methodology, Writing - original draft, Writing - review & editing. **J.P.K.:** Investigation, Formal analysis. **L.W.G.:** Investigation. **J.B.M.:** Investigation. **M.L.P.V.:** Investigation. **A.S.:** Investigation, Methodology, Data curation. L.d.C.: Investigation, Methodology, Data curation. **K.L.T.:** Conceptualization, Funding acquisition, Methodology, Project administration, Resources, Supervision, Writing - review & editing. **R.F.T.:** Conceptualization, Funding acquisition, Methodology, Project administration, Resources, Supervision, Writing - review & editing.

## Declaration of Competing Interest

The authors declare that they have no known competing financial interests or personal relationships that could have appeared to influence the work reported in this paper.

## Acknowledgements

We acknowledge the support of ANSTO in providing the neutron facilities used in this work. The work was supported by an AINSE PGRA award (C.S.G.B), and by an Australian Research Council Future Fellowship (FT160100191, R.F.T).

## Appendix A. Supplementary material

Supplementary data associated with this article can be found, in the online version, at https://doi.org/10.1016/j.jcis.2021.02.061.

## References

[1] J.Y. Shin, N.L. Abbott, Using light to control dynamic surface tensions of aqueous solutions of water soluble surfactants, Langmuir 15 (13) (1999) 4404–4410, https://doi.org/10.1021/la981477f.
[2] J. Liu, Y. Lu, Stimuli-responsive disassembly of nanoparticle aggregates for light-up colorimetric sensing, J. Am. Chem. Soc. 127 (36) (2005) 12677–12683, https://doi.org/10.1021/ja053567u.
[3] S.M. Mirvakili, I.W. Hunter, Artificial muscles: mechanisms, applications, and challenges, Adv. Mater. 30 (6) (2018) 1704407, https://doi.org/10.1002/adma.201704407.

[4] P.J. Roth, A.B. Lowe, Stimulus-responsive polymers, Polym. Chem. 8 (1) (2017) 10–11, https://doi.org/10.1039/C6PY90169G.
[5] Y. Zhang, Z. Chu, C.A. Dreiss, Y. Wang, C. Fei, Y. Feng, Smart wormlike micelles switched by $CO_2$ and air, Soft Matter 9 (27) (2013) 6217–6221, https://doi.org/10.1039/C3SM50913C.
[6] T. Wolff, C.S. Emming, T.A. Suck, G. Von Buenau, Photorheological effects in micellar solutions containing anthracene derivatives: A rheological and static low angle light scattering study, J. Phys. Chem. 93 (12) (1989) 4894–4898, https://doi.org/10.1021/j100349a043.
[7] D. Binder, A. Grünberger, A. Loeschcke, C. Probst, C. Bier, J. Pietruszka, W. Wiechert, D. Kohlheyer, K.-E. Jaeger, T. Drepper, Light-responsive control of bacterial gene expression: Precise triggering of the lac promoter activity using photocaged IPTG, Integr. Biol. (Camb) 6 (8) (2014) 755–765, https://doi.org/10.1039/c4ib00027g.
[8] C.S. Linsley, B.M. Wu, Recent advances in light-responsive on-demand drug-delivery systems, Ther. Deliv. 8 (2) (2017) 89–107, https://doi.org/10.4155/tde-2016-0060.
[9] M. Bradley, B. Vincent, N. Warren, J. Eastoe, A. Vesperinas, Photoresponsive surfactants in microgel dispersions, Langmuir 22 (1) (2006) 101–105, https://doi.org/10.1021/la0523053.
[10] J. Eastoe, A. Vesperinas, Self-assembly of light-sensitive surfactants, Soft Matter 1 (5) (2005) 338–347, https://doi.org/10.1039/B510877M.
[11] V.S. Molchanov, O.E. Philippova, A.R. Khokhlov, Y.A. Kovalev, A.I. Kuklin, Self-assembled networks highly responsive to hydrocarbons, Langmuir 23 (1) (2007) 105–111, https://doi.org/10.1021/la061612l.
[12] H. Shi, Y. Wang, B. Fang, Y. Talmon, W. Ge, S.R. Raghavan, J.L. Zakin, Light-responsive threadlike micelles as drag reducing fluids with enhanced heat-transfer capabilities, Langmuir 27 (10) (2011) 5806–5813, https://doi.org/10.1021/la200080w.
[13] P.G. Mazzola, A.M. Lopes, F.A. Hasmann, A.F. Jozala, T.C. Penna, P.O. Magalhaes, C.O. Rangel-Yagui, A.P. Jr, Liquid–liquid extraction of biomolecules: An overview and update of the main techniques, J. Chem. Technol. Biot. 83 (2) (2008) 143–157, https://doi.org/10.1002/jctb.1794.
[14] X. Gao, F. Lu, B. Dong, Y. Liu, Y. Gao, L. Zheng, Facile synthesis of gold and gold-based alloy nanowire networks using wormlike micelles as soft templates, ChemComm 51 (5) (2015) 843–846, https://doi.org/10.1039/C4CC08549C.
[15] A.M. Ketner, R. Kumar, T.S. Davies, P.W. Elder, S.R. Raghavan, A simple class of photorheological fluids: surfactant solutions with viscosity tunable by light, J. Am. Chem. Soc. 129 (6) (2007) 1553–1559, https://doi.org/10.1021/ja065053g.
[16] N. Müller, T. Wolff, G. von Bünau, Light-induced viscosity changes of aqueous solutions containing 9-substituted anthracenes solubilized in cetyltrimethylammonium micelles, J. Photoc. 24 (1) (1984) 37–43, https://doi.org/10.1016/0047-2670(84)80004-0.
[17] A. Matsumura, K. Sakai, H. Sakai, M. Abe, Photoinduced increase in surfactant solution viscosity using azobenzene dicarboxylate for molecular switching, J. Oleo Sci. 60 (5) (2011) 203–207, https://doi.org/10.5650/jos.60.203.
[18] Z. Chu, C.A. Dreiss, Y. Feng, Smart wormlike micelles, Chem. Soc. Rev. 42 (17) (2013) 7174–7203, https://doi.org/10.1039/C3CS35490C.
[19] J.N. Israelachvili, D.J. Mitchell, B.W. Ninham, Theory of self-assembly of hydrocarbon amphiphiles into micelles and bilayers, J. Chem. Soc. Faraday Trans. 72 (1976) 1525, https://doi.org/10.1039/f29767201525.
[20] B. Song, Y. Hu, J. Zhao, A single-component photo-responsive fluid based on a gemini surfactant with an azobenzene spacer, J. Colloid Interface Sci. 333 (2) (2009) 820–822, https://doi.org/10.1016/j.jcis.2009.02.030.
[21] E.A. Kelly, N. Willis-Fox, J.E. Houston, C. Blayo, G. Divitini, N. Cowieson, R. Daly, R.C. Evans, A single-component photorheological fluid with light-responsive viscosity, Nanoscale 12 (11) (2020) 6300–6306, https://doi.org/10.1039/C9NR10350C.
[22] H.M.D. Bandara, S.C. Burdette, Photoisomerization in different classes of azobenzene, Chem. Soc. Rev. 41 (5) (2012) 1809–1825, https://doi.org/10.1039/C1CS15179G.
[23] E. Merino, Synthesis of azobenzenes: The coloured pieces of molecular materials, Chem. Soc. Rev. 40 (7) (2011) 3835–3853.
[24] F. Liu, M. Xu, X. Chen, Y. Yang, H. Wang, G. Sun, Novel strategy for tracking the microbial degradation of azo dyes with different polarities in living cells, Environ. Sci. Technol. 49 (19) (2015) 11356–11362, https://doi.org/10.1021/acs.est.5b02003.
[25] G.S. Kumar, D.C. Neckers, Photochemistry of azobenzene-containing polymers, Chem. Rev. 89 (8) (1989) 1915–1925, https://doi.org/10.1021/cr00098a012.
[26] C. Rosslee, N.L. Abbott, Active control of interfacial properties, Curr. Opin. Colloid Interface Sci. 5 (1) (2000) 81–87, https://doi.org/10.1016/S1359-0294(00)00035-2.
[27] M. Akamatsu, M. Shiina, R. Goswami Shrestha, K. Sakai, M. Abe, H. Sakai, Photoinduced viscosity control of lecithin-based reverse wormlike micellar systems using azobenzene derivatives, RSC Adv. 8 (42) (2018) 23742–23747, https://doi.org/10.1039/C8RA04690E.
[28] F.P. Hubbard, N.L. Abbott, Effect of light on self-assembly of aqueous mixtures of sodium dodecyl sulfate and a cationic, bolaform surfactant containing azobenzene, Langmuir 23 (9) (2007) 4819–4829, https://doi.org/10.1021/la0632124.
[29] Y. Hu, J.B. Marlow, R. Ramanathan, W. Zou, H.G. Tiew, M.J. Pottage, V. Bansal, R. F. Tabor, B.L. Wilkinson, Synthesis and properties of photoswitchable carbohydrate fluorosurfactants, Aust. J. Chem. 68 (12) (2016) 1880–1884, https://doi.org/10.1071/CH15434.
[30] Y. Hu, W. Zou, V. Julita, R. Ramanathan, R.F. Tabor, R. Nixon-Luke, G. Bryant, V. Bansal, B.L. Wilkinson, Photomodulation of bacterial growth and biofilm formation using carbohydrate-based surfactants, Chem. Sci. 7 (11) (2016) 6628–6634, https://doi.org/10.1039/C6SC03020C.
[31] R.F. Tabor, D.D. Tan, S.S. Han, S.A. Young, Z.L.E. Seeger, M.J. Pottage, C.J. Garvey, B.L. Wilkinson, Reversible pH- and photocontrollable carbohydrate-based surfactants, Chem. Eur. J. 20 (43) (2014) 13881–13884, https://doi.org/10.1002/chem.201404945.
[32] A. Sokolova, J. Christoforidis, A. Eltobaji, J. Barnes, F. Darmann, A.E. Whitten, L. de Campo, BILBY: time-of-flight small angle scattering instrument, Neutron News 27 (2) (2016) 9–13, https://doi.org/10.1080/10448632.2016.1163980.
[33] A. Sokolova, A.E. Whitten, L. de Campo, J. Christoforidis, A. Eltobaji, J. Barnes, F. Darmann, A. Berry, Performance and characteristics of the BILBY time-of-flight small-angle neutron scattering instrument, J. Appl. Cryst. 52 (1) (2019) 1–12, https://doi.org/10.1107/S1600576718018009.
[34] C. Rehm, A. Brûlé, A.K. Freund, S.J. Kennedy, Kookaburra: The ultra-small-angle neutron scattering instrument at OPAL, J. Appl. Cryst. 46 (6) (2013) 1699–1704, https://doi.org/10.1107/S0021889813025788.
[35] C. Rehm, L. de Campo, KOOKABURRA: the ultra-small-angle neutron scattering instrument at ANSTO, Neutron News 27 (2) (2016) 30–32, https://doi.org/10.1080/10448632.2016.1165063.
[36] C. Rehm, L. de Campo, A. Brûlé, F. Darmann, F. Bartsch, A. Berry, Design and performance of the variable-wavelength Bonse-Hart ultra-small-angle neutron scattering diffractometer KOOKABURRA at ANSTO, J. Appl. Crystallogr. 51 (1) (2018) 1–8, https://doi.org/10.1107/S1600576717016879.
[37] J.D. Berry, M.J. Neeson, R.R. Dagastine, D.Y.C. Chan, R.F. Tabor, Measurement of surface and interfacial tension using pendant drop tensiometry, J. Colloid Interface Sci. 454 (2015) 226–237, https://doi.org/10.1016/j.jcis.2015.05.012.
[38] M. Montagna, O. Guskova, Photosensitive cationic azobenzene surfactants: thermodynamics of hydration and the complex formation with poly (methacrylic acid), Langmuir 34 (1) (2018) 311–321, https://doi.org/10.1021/acs.langmuir.7b03638.
[39] B.E. Rapp, Chapter 20 - Surface Tension, in: B.E. Rapp (Ed.), Microfluidics: Modelling, Mechanics and Mathematics, Micro and Nano Technologies, Elsevier, Oxford, 2017, pp. 421–444, https://doi.org/10.1016/B978-1-4557-3141-1.50020-4.
[40] P. Debye, E.W. Anacker, Micelle shape from dissymmetry measurements, J. Phys. Chem. 55 (5) (1951) 644–655, https://doi.org/10.1021/j150488a003.
[41] R. Kumar, G.C. Kalur, L. Ziserman, D. Danino, S.R. Raghavan, Wormlike Micelles of a C22-tailed zwitterionic betaine surfactant: from viscoelastic solutions to elastic gels, Langmuir 23 (26) (2007) 12849–12856, https://doi.org/10.1021/la7028559.
[42] V.T. Kelleppan, J.E. Moore, T.M. McCoy, A.V. Sokolova, L. de Campo, B.L. Wilkinson, R.F. Tabor, Self-Assembly of long-chain betaine surfactants: effect of tailgroup structure on wormlike micelle formation, Langmuir 34 (3) (2018) 970–977, https://doi.org/10.1021/acs.langmuir.7b02830.
[43] J.E. Hunter, J.F. Fowler, Safety to human skin of cocamidopropyl betaine: A mild surfactant for personal-care products, J. Surfact. Deterg. 1 (2) (1998) 235–239, https://doi.org/10.1007/s11743-998-0025-3.
[44] M.T. Garcia, E. Campos, A. Marsal, I. Ribosa, Fate and effects of amphoteric surfactants in the aquatic environment, Environ. Int. 34 (7) (2008) 1001–1005, https://doi.org/10.1016/j.envint.2008.03.010.
[45] J.E. Houston, E.A. Kelly, M. Kruteva, K. Chrissopoulou, N. Cowieson, R.C. Evans, Multimodal control of liquid crystalline mesophases from surfactants with photoswitchable tails, J. Mater. Chem. C 7 (35) (2019) 10945–10952, https://doi.org/10.1039/C9TC04079J.
[46] J.E. Moore, T.M. McCoy, L. de Campo, A.V. Sokolova, C.J. Garvey, G. Pearson, B.L. Wilkinson, R.F. Tabor, Wormlike micelle formation of novel alkyl-tri(ethylene glycol)-glucoside carbohydrate surfactants: Structure–function relationships and rheology, J. Colloid Interface Sci. 529 (2018) 464–475, https://doi.org/10.1016/j.jcis.2018.05.060.
[47] R. Nagarajan, Molecular packing parameter and surfactant self-assembly: the neglected role of the surfactant tail, Langmuir 18 (1) (2002) 31–38, https://doi.org/10.1021/la010831y.
[48] J.M. Kuiper, J.B.F.N. Engberts, H-aggregation of azobenzene-substituted amphiphiles in vesicular membranes, Langmuir 20 (4) (2004) 1152–1160, https://doi.org/10.1021/la0358724.
[49] M. Shimomura, R. Ando, T. Kunitake, Orientation and spectral characteristics of the azobenzene chromophore in the ammonium bilayer assembly, Ber. Bunsenges. Phys. Chem. 87 (12) (1983) 1134–1143, https://doi.org/10.1002/bbpc.19830871211.
[50] M. Kasha, Energy transfer mechanisms and the molecular exciton model for molecular aggregates, Radiat. Res. 20 (1) (1963) 55–70.
[51] M. Shimomura, T. Kunitake, Fusion and phase separation of ammonium bilayer membranes, Chem. Lett. 10 (7) (1981) 1001–1004, https://doi.org/10.1246/cl.1981.1001.
[52] M.T. Meftah, H. Gossa, K.A. Touati, K. Chenini, A. Naam, Doppler broadening of spectral line shapes in relativistic plasmas, Atoms 6 (2) (2018) 16, https://doi.org/10.3390/atoms6020016.
[53] S.P. Kwasniewski, J.P. François, M.S. Deleuze, Temperature effects on the UV–Vis electronic spectrum of trans-stilbene, Int. J. Quantum Chem. 85 (4–5) (2001) 557–568, https://doi.org/10.1002/qua.10016.
[54] J.C. Ted Lee, K.A. Smith, T.A. Hatton, Small-Angle Neutron Scattering Study of the Micellization of Photosensitive Surfactants in Solution and in the Presence of a Hydrophobically Modified Polyelectrolyte†, http://pubs.acs.org/doi/full/10.1021/la9016239 (Aug. 2009). doi:10.1021/la9016239.
[55] C.K. Wong, A.F. Mason, M.H. Stenzel, P. Thordarson, Formation of non-spherical polymersomes driven by hydrophobic directional aromatic perylene

interactions, Nat. Commun. 8 (1) (2017) 1–10, https://doi.org/10.1038/s41467-017-01372-z.
[56] T. Moldt, D. Brete, D. Przyrembel, S. Das, J.R. Goldman, P.K. Kundu, C. Gahl, R. Klajn, M. Weinelt, Tailoring the properties of surface-immobilized azobenzenes by monolayer dilution and surface curvature, Langmuir 31 (3) (2015) 1048–1057, https://doi.org/10.1021/la504291n.
[57] F.M. Menger, A.L. Galloway, Contiguous versus segmented hydrophobicity in micellar systems, J. Am. Chem. Soc. 126 (48) (2004) 15883–15889, https://doi.org/10.1021/ja040105s.
[58] T.M. McCoy, A. Valiakhmetova, M.J. Pottage, C.J. Garvey, L. de Campo, C. Rehm, D.A. Kuryashov, R.F. Tabor, Structural evolution of wormlike micellar fluids formed by erucyl amidopropyl betaine with oil, Salts, Surfactants, Langmuir 32 (47) (2016) 12423–12433, https://doi.org/10.1021/acs.langmuir.6b01735.
[59] R.D. Koehler, S.R. Raghavan, E.W. Kaler, Microstructure and dynamics of wormlike micellar solutions formed by mixing cationic and anionic surfactants, J. Phys. Chem. B 104 (47) (2000) 11035–11044, https://doi.org/10.1021/jp0018899.
[60] F. Kern, P. Lemarechal, S.J. Candau, M.E. Cates, Rheological properties of semidilute and concentrated aqueous solutions of cetyltrimethylammonium bromide in the presence of potassium bromide, Langmuir 8 (2) (1992) 437–440, https://doi.org/10.1021/la00038a020.
[61] N.N. Kochurova, E.R. Airapetova, N.G. Abdulin, O.P. Korotkikh, A.V. Lezov, G. Petzold, Viscosity of aqueous micellar solutions of surfactants, Colloid J. 74 (5) (2012) 564–568, https://doi.org/10.1134/S1061933X12050055.
[62] M. Takeda, T. Kusano, T. Matsunaga, H. Endo, M. Shibayama, T. Shikata, Rheo-SANS studies on shear-thickening/thinning in aqueous rodlike micellar solutions, Langmuir 27 (5) (2011) 1731–1738, https://doi.org/10.1021/la104647u.
[63] J.J. Hermans, P.H. Hermans, D. Vermaas, A. Weidinger, Quantitative evaluation of orientation in cellulose fibres from the X-ray fibre diagram, Recl. Trav. Chim. Pays-Bas 65 (6) (1946) 427–447, https://doi.org/10.1002/recl.19460650605.
[64] J.L. White, J.E. Spruiell, The specification of orientation and its development in polymer processing, Polym. Eng. Sci. 23 (5) (1983) 247–256, https://doi.org/10.1002/pen.760230503.
[65] G. Wiberg, M.L. Skytt, U.W. Gedde, Shear-induced alignment and relaxation of orientation in smectic side-chain liquid-crystalline polymers, Polymer 39 (13) (1998) 2983–2986, https://doi.org/10.1016/S0032-3861(97)00626-5.
[66] B. Tian, Z. Wang, L. de Campo, E.P. Gilbert, R.M. Dalgliesh, E. Velichko, A.J. van der Goot, W.G. Bouwman, Small angle neutron scattering quantifies the hierarchical structure in fibrous calcium caseinate, Food Hydrocolloids 106 (2020) 105912, https://doi.org/10.1016/j.foodhyd.2020.105912.
[67] B. Arenas-Gómez, C. Garza, Y. Liu, R. Castillo, Alignment of worm-like micelles at intermediate and high shear rates, J. Colloid Interface Sci. 560 (2020) 618–625, https://doi.org/10.1016/j.jcis.2019.10.052.
[68] A.F. Olea, J.K. Thomas, Rate constants for reactions in viscous media: Correlation between the viscosity of the solvent and the rate constant of the diffusion-controlled reactions, J. Am. Chem. Soc. 110 (14) (1988) 4494–4502, https://doi.org/10.1021/ja00222a002.
[69] R.E. McKinnie, J.S. Olson, Effects of solvent composition and viscosity on the rates of CO binding to heme proteins, J. Biol. Chem. 256 (17) (1981) 8928–8932.
[70] S. Cai, K. Vijayan, D. Cheng, E.M. Lima, D.E. Discher, Micelles of different morphologies–advantages of worm-like filomicelles of PEO-PCL in paclitaxel delivery, Pharm. Res. 24 (11) (2007) 2099–2109, https://doi.org/10.1007/s11095-007-9335-z.
[71] A.-L.M. Le Ny, C.T. Lee, Photoreversible DNA condensation using light-responsive surfactants, J. Am. Chem. Soc. 128 (19) (2006) 6400–6408, https://doi.org/10.1021/ja0576738.
[72] H. Ranchon, R. Malbec, V. Picot, A. Boutonnet, P. Terrapanich, P. Joseph, T. Leïchlé, A. Bancaud, DNA separation and enrichment using electro-hydrodynamic bidirectional flows in viscoelastic liquids, Lab Chip 16 (7) (2016) 1243–1253, https://doi.org/10.1039/C5LC01465D.
[73] F. Nettesheim, M.W. Liberatore, T.K. Hodgdon, N.J. Wagner, E.W. Kaler, M. Vethamuthu, Influence of nanoparticle addition on the properties of wormlike micellar solutions, Langmuir: ACS J. Surfaces Colloids 24 (15) (2008) 7718–7726, https://doi.org/10.1021/la800271m.
[74] M.E. Helgeson, T.K. Hodgdon, E.W. Kaler, N.J. Wagner, M. Vethamuthu, K.P. Ananthapadmanabhan, Formation and rheology of viscoelastic "double networks" in wormlike micelle-nanoparticle mixtures, Langmuir 26 (11) (2010) 8049–8060, https://doi.org/10.1021/la100026d.
[75] M. Zhao, Z. Gao, C. Dai, X. Sun, Y. Zhang, X. Yang, Y. Wu, Effect of silica nanoparticles on wormlike micelles with different entanglement degrees, J. Surfactants Deterg. 22 (3) (2019) 587–595, https://doi.org/10.1002/jsde.12252.